

Strain-based Spin Manipulation on Substitutional Nickel in Silicon Carbide

Wenhao Hu and Michael E. Flatté
 Department of Physics and Astronomy,
 The University of Iowa,
 Iowa City, Iowa 52242-1479 USA

(Dated: September 16, 2021)

By using the full potential linear augmented plane wave (FP-LAPW) method and full potential local orbital minimum basis (FP-LOMB) method within generalized gradient approximation (GGA), we studied the electronic structures and magnetic properties of nickel and chromium single dopants in polytypes of silicon carbide (SiC). The magnetic phases of defects are found to be strongly dependent on the external stress on the supercell. In 3C-SiC, the Ni single dopant exhibits an anti-ferromagnetic (AFM) to ferromagnetic (FM) transition at a moderate compressive and tensile hydrostatic strain in Si-sub and C-sub cases. In contrast, the Ni single dopant in 4H-SiC is stably in the nonmagnetic phase under external stress. The Cr single dopant is also insensitive to the applied stress but stably in the magnetic phase. This strain controlled magnetic transition makes the Ni single dopant a novel scheme of qubit.

PACS numbers:

I. INTRODUCTION

In the synthesis of diamond by high-pressure and high-temperature technique, transition metals are important catalysts to accelerate the conversion from graphite to diamond, during which the nickel complexes are incorporated into the diamond matrix in different forms. Through the demonstration of electron paramagnetic resonance, photoluminescence and optical absorption, numerous nickel-related defects has been identified in the diamond, including substitutional nickel¹, nickel-vacancy² and nickel-vacancy-nitrogen complexes (NE centers)³. Several theoretical approaches have been used to investigate these nickel-related defects' structural and electronic properties⁴⁻⁶. Experimentally, it has been reported that NE8 center can be an excellent infrared single-photon source at room temperature⁷⁻⁹.

In spite of that the NV center in diamond is an ideal candidate of qubit, it is still difficult to fabricate devices from diamond. In contrast, SiC is a wide-bandgap semiconductor with mature growth and device engineering technique. Commercial epitaxial and bulk monocrystal SiC are both available with high quality¹⁰. Intuitively, the single defect in SiC should have a long coherence time since the host atoms have stable spinless nuclear isotopes. In addition, the wide bandgap of SiC enables it to host various color centers.

But different from diamond, silicon carbide has various polytypes based on different stacking sequences of Si-C bilayer. More specifically, the atomic configuration of silicon carbide can be regarded as an alternating stack of two-dimensional Si and C layers. As shown in Fig.1, two different Si-C bilayers (h and k) are ordered in different patterns to produce 3C, 4H and 6H-SiC. Note that there will be many an inequivalent substitutional sites for both Si and C in hexagonal SiC. Thousands of structures of SiC have been discovered obeying above rules, of which 3C, 4H and 6H SiC are three of the most com-

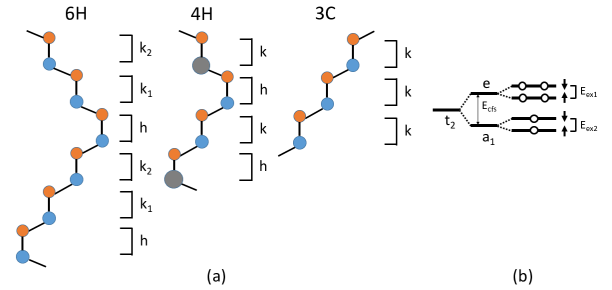


FIG. 1: (a) Sequence of SiC stack. (b) Crystal field splitting due to symmetry lowering.

mon polytypes. They have pervasive application in the power, opto-electronics and are also used as substrate of graphene¹¹ and gallium nitride¹². Combined with magnetic resonance measurement and numerical simulation, it is predicted recently that several defects in SiC is also possible to be competitive candidates as qubit¹³⁻¹⁶. For instance, it is recently demonstrated that there exists optical addressable spin states with long coherence times (5-50 μ s) at room temperature¹⁷. Double electron-electron resonance measurement in 6H-SiC proves the dipole-dipole coupling between spin ensembles, which is significant in practical spin-based quantum technologies. In this paper, we will investigate the possibility of realize universal manipulation of spin state of nickel dopant in polytypes of SiC with strain and microwave radiation.

This paper is organized as follows: In the Sec. II, we summarized the parameters and methods of our calculations in this paper and the relaxed geometries of nickel complexes. In addition, the Si-C charge transfer in SiC is also shown, which is a significant difference from diamond. Then, magnetic and electronic properties of substitutional nickel (Ni_s) in silicon site and carbon site under hydrostatic strain will be discussed. 3C (Sec. III A and III B) and 4H (Sec. III C) polytypes of silicon car-

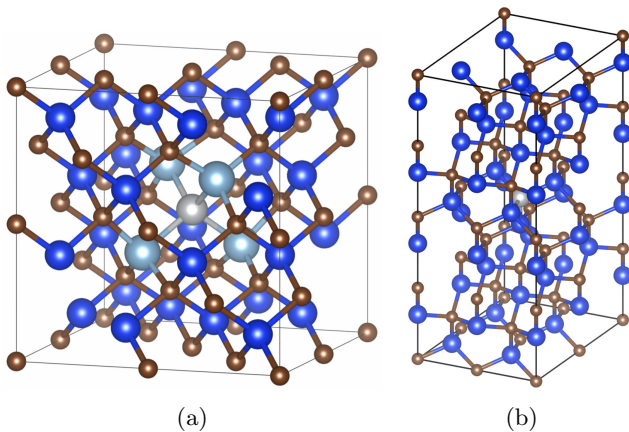


FIG. 2: Nickel doped (a) 3C and (b) 4H SiC supercells.

bide are both considered. Next, we will talk about the implementation scheme of Ni_s in SiC and its prospective directions to dig. In Sec. III D, we want to briefly talk about the electronic structure of chromium single dopant in 3C/4H-SiC. In the end, we will summarize our results and make a general comment in Sec. IV.

II. COMPUTATIONAL DETAILS

In our calculation, the FP-LAPW method implemented in WIEN2K package is exploited¹⁸. The PBE-GGA¹⁹ is used for the exchange correlation functional in the DFT self-consistent calculations. To achieve an accuracy of 1 meV in total energy, a $7 \times 7 \times 7$ Monkhorst-Pack k-mesh²⁰ is exploited. The cutoff energy is set up according to the product of minimum radius of muffin-tin and maximum wave vector $RK_{max} = 7.0$. Due to the periodic boundary condition used in the calculation, the interaction between neighboring unit cell need to be eliminated through the method of supercell. Considering the tradeoff between the limit of computational resource and accuracy, a $2 \times 2 \times 2$ supercell is considered. As shown in Fig.2, the impurity-contained supercells are $NiSi_xC_{63-x}$ ($x = 31$ or 32) supercells that consist of $2 \times 2 \times 2$ multiple of 3C (Fig.2a) and 4H (Fig.2b) SiC unit cells with a central nickel. The supercell size is determined according to experimental lattice constants of SiC: $a_{3c} = 4.3596 \text{ \AA}$, $a_{4h} = 3.0730 \text{ \AA}$ and $b_{4h} = 10.053 \text{ \AA}$. All the atoms are allowed to relax with a precision of $1\text{meV}/\text{\AA}$ according to T_d symmetry. The spin-orbital interaction is not included. In this paper, only hydrostatic strain is considered, which can be realized by proportionally extending or shrinking the volume of supercell.

There are two main differences between diamond and SiC. Firstly, SiC has two inequivalent substitutional sites, i.e. the silicon site and carbon site. Despite of the same symmetry, the wave function of nickel's $3d$ electron will have a smaller overlap with NN carbon's dangling bond than NN silicon's dangling bond. Compared with dia-

mond, the larger size of a silicon atom suppresses the spreading of nickel's electronic wave function while the looser relaxation space of nickel's central tetrahedron provides an additional tensile hydrostatic strain. Therefore, we expect this spin center to exhibit a higher transition strain than Ni_s in diamond²¹, especially C-sub Ni in SiC.

Secondly, Si and C both have four electrons in the outermost subshell and share the same symmetry in the SiC matrix. Nevertheless, the difference in Si and C's electronegativities leads to a charge transfer between them. Before calculating the impurity-contained SiC supercell, the pure 4H and 3C SiC supercells are checked with FP-LOMB, which is implemented in FPLO package²², to investigate the charge transfer between Si and C. Note that WIEN2K is implemented with LAPW method so that it's unable to evaluate the precise occupation information. The calculated Si \rightarrow C charge transfers are shown in the following table: It can be seen that the silicon atoms give

3C-SiC		
Atom	Q-tot	Q-excess
C	7.032	1.032
Si	12.968	-1.032
4H-SiC		
Atom	Q-tot	Q-excess
C	7.053	1.053
Si	12.947	-1.053

TABLE I: Si \rightarrow C charge transfers in 3C and 4H SiC.

away 1.03-1.05 electrons/atom to carbon atoms so that the ionic formula for SiC becomes $Si^{+1.04}C^{-1.04}$. This result is 0.3 electrons/atom off that in²³, which is due to the difference in functionals we use. The charge transfer mainly occurs in the formation of Si-C bond, which is about 0.26 electrons/bond. The excess charge in carbon atoms makes the difference between local environment of impurities in diamond and SiC not only the atomic separation, but the on-site coulomb potential.

III. RESULTS

A. Carbon substituted nickel in 3C silicon carbide

With above setup, the C-sub Ni_s is investigated. Considering the odd number occupation of $3d$ electron in nickel, we investigated the effect of Jahn-Teller distortion first by allowing a $P1$ symmetric atomic relaxation. Compared with T_d symmetric relaxation, only a difference of 0.09 eV in the total energy is observed. For simplicity, the relaxation is constrained to T_d symmetry in C-sub case. Under ambient pressure, the whole unit cell is anti-ferromagnetic (AFM). As the lattice constant is extended by 6%, the antiferromagnetic-ferromagnetic transition shows up, which is similar to the result in²¹.

This bonding mechanism between Ni and nearest neighbor (NN) Si can be explained via the $p-d$ hybridization model. Under the crystal field, the degeneracy of $3d$ is lowered and splitted into t_2 and e orbitals, which have a degeneracy of three and two respectively. t_2 orbital approaches the silicon along the Si-Ni axis which can form sigma bonds with ligands so that it locates above the e orbitals. The dangling bonds with $3s3p$ character are splitted into a_1 and t_2 level, which can hybridize with the $3d$ derived t_2 level. The orbital partial occupation is listed as follows:

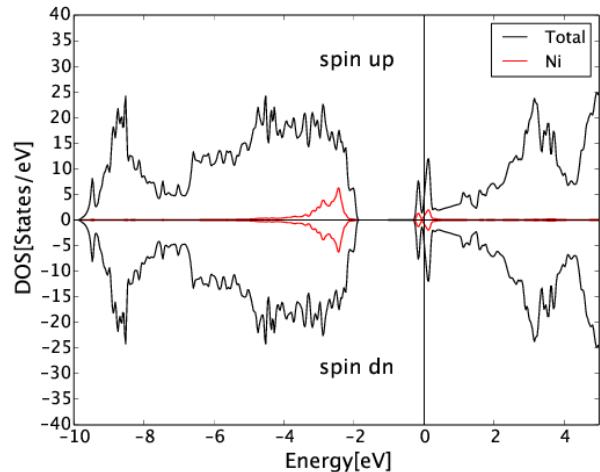
	3s	3p	4s	5s	3d	4d	4p
Ni _s	2.000	6.007	0.628	-0.003	8.731	0.106	0.518
Ni _s spin	0	0	0.015	0.001	0.306	-0.008	0.202
	2s	2p	3s	4s	3p	4p	3d
NN Si	2.000	6.000	1.149	-0.009	2.056	-0.022	0.369
NN Si spin	0	0	0.033	0	0.178	0.002	0.026

TABLE II: Projected occupation and spin of Ni_s and NN silicon.

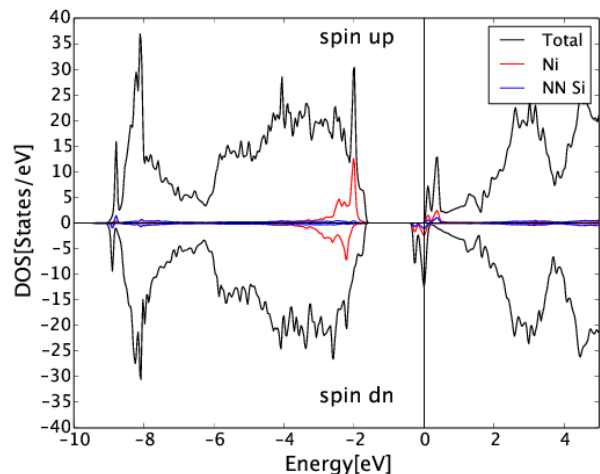
Before looking into the detailed population and spin configuration, we need to note that the occupation here is a result of hybridization between levels with the same symmetry. In other words, it cannot offer a precise description on the electron configuration before hybridization. To recover the pre-hybridized configuration, we need to sort the orbitals according to their symmetries.

The closed shell electrons, including $3s_{\text{Ni}}$, $3p_{\text{Ni}}$, $2s_{\text{Si}}$ and $2p_{\text{Si}}$, won't participate the formation of bonds. The $4s_{\text{Ni}}$ and $3s_{\text{Si}}$ give rise to a_1 hybrid orbital, while the $3d_{\text{Ni}}$, $3p_{\text{Si}}$, $4p_{\text{Ni}}$ and $3d_{\text{Si}}$ form t_2 level. Note that part of the $3d_{\text{Ni}}$ electrons will be splitted into an e level due to the crystal field as before. As a result, $1.76(\approx 2)$ electrons and $7.677(\approx 8)$ electrons will occupy the $4s/3s$ derived a_1 and $3d_{\text{Ni}}/4p_{\text{Ni}}/3p_{\text{Si}}/3d_{\text{Si}}$ derived t_2 level respectively. Regarding the a_1 level, both of the $4s_{\text{Ni}}$ and $3s_{\text{Si}}$ electrons are spinless, which indicates the full occupation of the bonding and anti-bonding a_1 . As for the t_2 level, we can take the Ni atom as a reference. Ni typically exhibits a configuration of $3d^9 4s^1$. Both of the $4p_{\text{Ni}}$ and $3d_{\text{Si}}$ levels are far above the outermost electron in Ni and Si atoms. Although they are partially occupied, they are still supposed to be empty before hybridization. Therefore, the electron assignments will be $3d^9$ and $3p^3$, in which $3p^3$ exhibits $\uparrow\downarrow$ configuration to achieve a polarized subshell. Here, the unquantized d shell occupation can actually be attributed to the mixing of $3d^9$ and $3d^8$ as the result of transition metals on the $\text{Cu}_2\text{N}/\text{Cu}(100)$ interface²⁴.

As will be discussed later, Si-sub and C-sub Ni_s essentially have the same bonding mechanism while the C-sub case has a higher occupation in Ni site. The main reason for this difference is the polarization of $4s$ orbital between Ni_s and NN silicon. In spite of the same configuration, $4s$ orbital is less extensive due to the lower electronegativity of silicon so that Ni_s will appear as a neutral atom. Therefore, both of dangling bond and Ni_s



(a)



(b)

FIG. 3: Total density of states and partial density of states of nickel and nearest-neighbor silicon of C-sub case under 4% (a) and 8% (b) tensile strain.

have a net magnetic moment of $1 \mu_B$. Other than that, the deviation of silicon's occupation from neutral indicates the polarization in Si-C bonds.

As shown in Fig.3a, we can see the total and nickel's partial DOS under 4% strain. Due to the absence of a magnetic moment, a symmetric spin configuration can be observed straightforwardly. Near the conduction band edge, we can see a partially occupied antibonding level locating at 2 eV above the valence band maximum (VBM), which is attributed to Ni's $3d$ electron and dangling bonds. About 0.5 eV below the VBM, e levels can be observed. Here, the defect level adjoins and extends into conduction band, which is due to the underestimation of the SGGA functional. The calculated bandgap of defect-free 3C-SiC under ambient strain is 1.362 eV compared with the experimental value of 2.36 eV.

For comparison, we show the total and nickel's partial DOS under 8% strain in Fig.3b. The electronic structure exhibits Stoner behaviour with an asymmetry in the spin-up and spin-down channels. Around 2 eV and 1.8 eV above VBM, two anti-bonding levels are formed by the $2p_{\text{Si}}^2$ and $3d_{\text{Ni}}^{10}$ derived t_2 levels, of which one is partially occupied and the other one is empty. The two spin-up anti-bonding electrons render the whole unit cell ferromagnetic. Again, we can see two $3d$ derived e levels around 0.3 eV below the VBM, while they are separated by a Hund exchange splitting $J = 0.1$ eV.

The bonding mechanism for the AFM and FM phases are summarized with a diagram in Fig.4. For simplicity, we neglect some levels that participate in the hybridization but only make minor contributions. Apparently, the spin splitting in $3d$ level derived crystal field levels will only happen in the FM phase but not the AFM phase. This diagram also identifies the origin of the ferromagnetism, namely the exchange interaction between the $\frac{1}{2}$ -spin residing in dangling bond and that in nickel transfer from dangling bond. The Heisenberg exchange coupling $J_H = (E_{\text{AFM}} - E_{\text{FM}})$ between these neighboring $\frac{1}{2}$ spins stabilizes the parallel alignment. The strain-dependent exchange coupling energy is evaluated and shown in Fig.5. To calculate the total energy of metastable states with a magnetic phase different from ground states, we made constrained DFT calculations with the magnetic moment fixed to the value of interest. The total energy is minimized with the constrained magnetic moment. The exchange coupling energy varies linearly as the strain with a slope of 11.2 meV/%. Note that the Heisenberg exchange energy per atom is within 10 meV. In the diluted magnetic semiconductor, the atomic disorder of the host atom and impurity caused by unnegligible entropy will cause the reversal of magnetic states at finite temperature²⁵. However, the result we achieve here is from a single dopant rather than diluted doped, which means the group disorder won't have an impact on the single impurity.

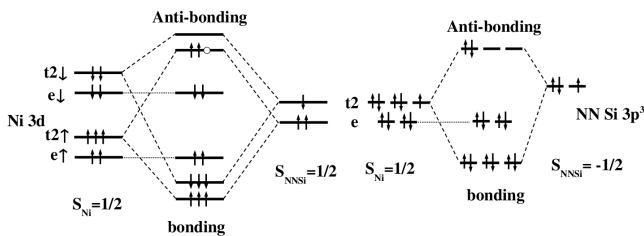


FIG. 4: Hybridization between Ni and NN silicon in FM(left) and AFM(right) phase.

To describe the C-sub Ni_s spin center, we treat it as a system consists of two local $\frac{1}{2}$ -spins, in which the coupling strength can be manipulated with strain. The spin Hamiltonian can be written as

$$H = -2JS_{\text{Ni}} \cdot \mathbf{S}_d + g_{\text{Ni}}\mu_{\text{Ni}}B_z S_{\text{Ni}z} + g_d\mu_d B_z S_{dz}. \quad (1)$$

Here, the external magnetic field B_z splits off the $T_{+/-}$ so as to orient the magnetic moment of unit cell. By selecting the triplet $T_0(s = 1, s_z = 0)$ and singlet S as the logical qubits, we can create a decoherence-free space immune from collective dephasing. In the representation of T_0/S , the spin Hamiltonian can be written as

$$H = \begin{bmatrix} -J/2 & \mu_B B_z \Delta g/2 \\ \mu_B B_z \Delta g/2 & J/2 \end{bmatrix}, \quad (2)$$

where $\Delta g = g_{\text{Ni}} - g_d$.

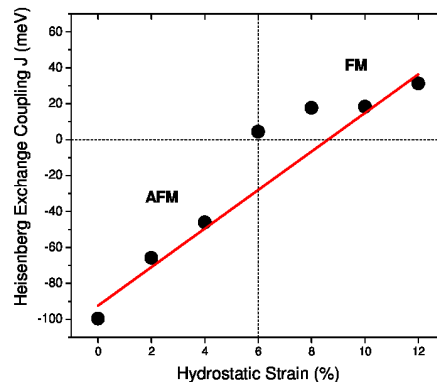


FIG. 5: Heisenberg exchange between the two spins localized to nickel and surrounding silicons in the C-sub case.

Due to the delocalization of the dangling bond, we can use the g-factor of free electron to describe it. As for nickel, we need to know the total angular momentum and orbital angular momentum of the holes in d shell. In reality, there is a predominant spin-orbital interaction in nickel which splits the $3d$ derived t_2 further. t_2 can be spanned in the space of d_{xz} , d_{yz} and d_{xy} , which can form orbitals with $m = +1, 0, -1$. Note that the $m = 0$ orbital is a mix of $m = 2$ and $m = -2$ orbitals. Due to the spin-orbital coupling, the holes occupy the highest level which is parallel to the spin. We can get the total angular momentum $J = 3/2$ and $g_1 = 1.33$.

In Chanier *et al.*'s work, they proposed a model of Hund's rule driven hopping between the pair of spins in Ni and the dangling bond, which is also applicable in our problem²¹. As shown in Fig.6, the varying Ni-NN distance due to the applied strain change the probability of virtual hopping between nickel and NN silicon. According to double-exchange model, a spin possesses a lower kinetic energy if it can hop between two potential wells without changing its spin direction. This contribution to the exchange energy depends on the hopping and on-site coulomb interaction:

$$E_{\text{hop}} \propto -\frac{t^2}{U}. \quad (3)$$

The hopping probability inversely depends on the spatial separation R and energy separation W between the

occupied states²⁶

$$P \sim \exp[-2\alpha R - \frac{W}{kT}]. \quad (4)$$

Therefore, the varying Ni-NN distance effects the $3d_{\text{Ni}}-sp_{\text{NN}}$ hopping strength so as to induce this AFM-FM transition.

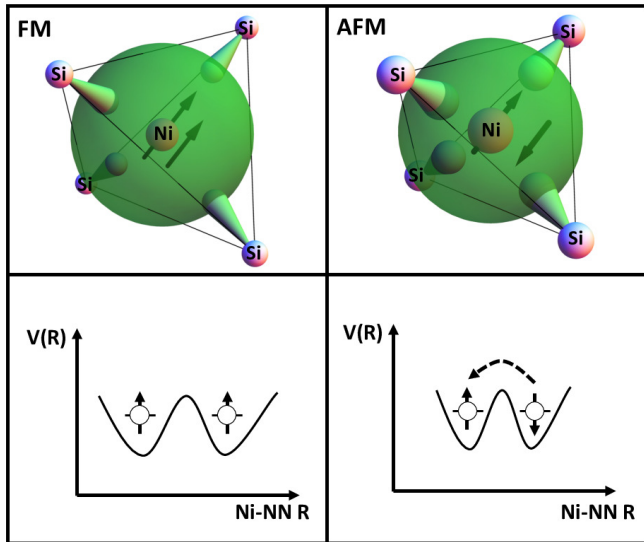


FIG. 6: Virtual hopping induced AFM-FM transition due to the Ni-NN distance.

B. Silicon substituted nickel in 3C silicon carbide

The strain effect on the magnetic states of Si-sub nickel in 3C-SiC is also investigated. The $P1$ symmetry relaxation check shows that the total energy is only 0.5 eV stabler than that under T_d symmetry due to Jahn-Teller distortion. NN carbon is distorted closer to the impurity by 0.003 Å. As a result, the structure optimization will obey T_d symmetry only. Hydrostatic strain from compressive 15% to tensile 2% have been considered. Due to the similar size of nickel and silicon, the NN carbons are pushed out along diagonal direction by only 1%. Compared with Ni_s in diamond(14%), this results implies a much lower formation energy. Also, this equivalent built-in tensile strain indicates a much larger strain is required to realize the antiferromagnetic(AFM)-ferromagnetic (FM) transition.

Similarly, the $p-d$ hybridization model can be used to describe our calculation. We calculated the total and projected occupation of nickel and NN carbon with the method of FP-LOMB. The occupations are shown in the Table.III. As a result of the big difference in the electronegativity between C and Ni, the outmost 4s electron of Ni is attracted by the dangling bond of NN carbon, which is verified by the total occupation of 27.2 for Ni_s . Consequently, Ni_s exhibits an electron configuration of

$3d^9 4s^0$ while the dangling bond is in $2s^2 2p^3$ configuration. Before the dangling bond hybridize with Ni_s , there is a $1 \mu_B$ net magnetic moment residing in both of them. After the crystal field splitting, the derived level is as shown in Fig.7. With the same symmetry, the $3d_{\text{Ni}}$ derived t_2 hybridizes with $2p_{\text{NN}}$ derived t_2 to form an anti-bonding level (t_{AB}) and bonding (t_B) level.

	3s	3p	4s	5s	3d	4d	4p
Ni_s	1.999	6.004	0.452	-0.010	8.421	0.096	0.522
Ni_s spin	0	-0.003	0.012	0	0.879	-0.016	0.116
	1s	2s	3s	2p	3p	3d	
NN C	2.000	1.374	0.001	3.215	-0.003	0.023	
NN C spin	0	0.014	0	0.159	0.001	0.002	

TABLE III: Projected occupations of Ni_s and NN carbon.

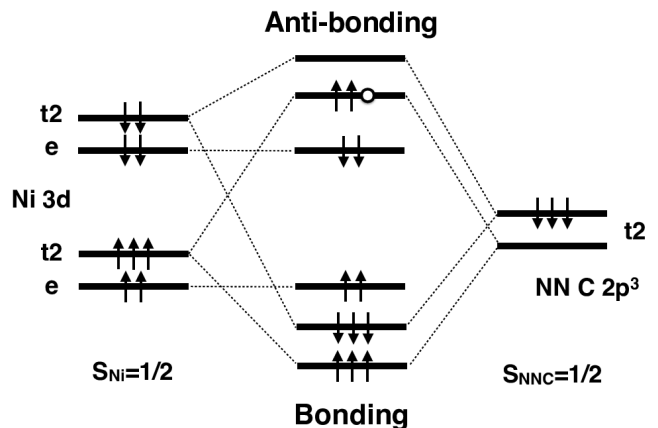


FIG. 7: Hybridization between Ni's 3d electrons and NN carbon's dangling bond.

The dependence of J on the hydrostatic strain is shown in Fig.8. As the compressive strain is raised above 10%, an AFM-FM transition can be observed. According to the stiffness tensor of 3C-SiC²⁷, this strain is equivalent to a pressure ~ 114 GPa, which can be achieved by using diamond anvil cell²⁸. This result also confirms our prediction of a higher transition strain since the Ni-NN spatial separation is larger in SiC. To initialize qubits, a compressive strain can be used to prepare it in the T_+ since it's in the FM phase. Then a microwave radiation can coherently manipulate the spin into T_0 state. After initialization, we can realize arbitrary one-qubit operations by strain-based and applied magnetic field according to Eq. 2.

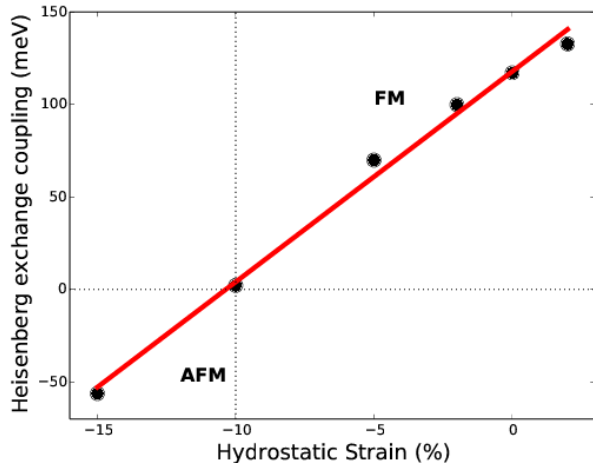


FIG. 8: Heisenberg exchange between the two spins localized to Ni and surrounding carbons in the Si-sub case.

C. Nickel in 4H silicon carbide

After discussing on cubic SiC, we want to look into one of the most important hexagonal SiC polytypes, namely 4H-SiC. There are two inequivalent Si and C sites in 4H-SiC as shown in Fig.1. However, the substitutional sites has minor impact on the electronic property²⁹ due to the similarity in their local environment so that only h site is considered in our work. The applied hydrostatic strain is adjusted from -10% to +6%. To achieve an accuracy of 10 meV, a $4 \times 4 \times 4$ Monkhorst-Pack k-mesh is used.

The AFM and FM solutions are obtained through magnetic moment constrained calculation. The discrepancy between the AFM and FM phases (within 100 meV) shows that the Heisenberg exchange coupling is not sensitive to the strain and close to the thermal energy at room temperature. In thermodynamic equilibrium, its statistical distribution can be described by Maxwell-Boltzmann equation:

$$\frac{n_{FM}}{n_{AFM}} = e^{-\frac{E_H}{kT}}, \quad (5)$$

where the E_H is the Heisenberg exchange energy. This ratio is around 0.607 at room temperature, which implies that AFM and FM states can exist concurrently. Except for the AFM ground state, we also observed an unstable magnetic local minimum (total magnetic moment of $0.6 \mu_B$) with tensile strain, which should be a mixed state of AFM and FM phases. A nonzero tunnelling probability between these configurations gives rise to this noninteger magnetic moment, which is similar to the anomalous thermal properties of glasses below 1K³⁰. The lower-energy curve are both the nonmagnetic solution while the higher-energy are both the magnetic solution.

After atomic position optimization, we can see that the C-sub case is relaxed to a much larger extent compared

with Si-sub case (Fig.9). Due to that the radius of Ni and Si are similar, the Ni-NN distance increases linearly in Si-sub case. In contrast, the relaxation of Ni-NN distance from the undoped and strained SiC:

$$D = d_{\text{Ni-NN}} - d_{\text{Si-C}} \quad (6)$$

reaches the maximum at -8% to -6% compressive strain. Compared with the lateral NN atom, the medial NN atom in both cases have a larger relaxation, whose unpaired p_z electron gives rise to the CFS a_1 as shown in Fig.1. This pattern agrees well with the level configuration derived from the group theory.

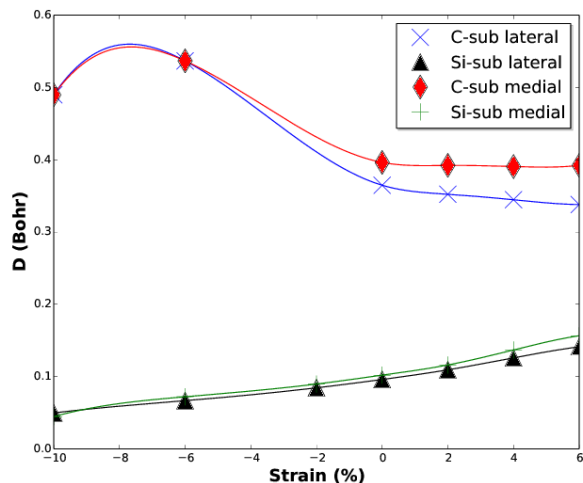


FIG. 9: Volume dependence of Ni-NN relaxation in ferromagnetic and anti-ferromagnetic states.

The detailed population of Ni and its NN atoms via LOMB method are listed in the table IV. Due to the charge transfer between silicon and carbon atom, nickel carries a more accurate information here. The hybridized 3d shell of nickel consists of $3d$, $4d$ and $4p$ orbitals, which gives a total 3d occupation of 9.089 and 9.454 in the Si-sub and C-sub cases. These orbitals form a_1 and e hybridized levels ($d_{z^2} \rightarrow a_1$, $\{\{d_{xz}, d_{yz}\}, \{d_{xy}, d_{x^2-y^2}\}\} \rightarrow e$) together with NN-Si/C's $3s3p/2s2p$, which have the same symmetry. Other than that, the occupation of 3d shell indicates that the nickel is in the +1 valence state in Si-sub case while the mixed state of +1 and neutral state in C-sub case.

To verify the electronic configuration of impurity and complex, the total and partial density of states in C and Si substituted SiC are shown in Fig.10a and Fig.10b. In C-sub case, the defect level extends to the conduction band, which should disappear if the band gap issue is fix. In Si-sub case, the defect band is located near the top of the host's valence band. Differently, the defect band is located near the top of the host's valence band in Si-sub case. This is mainly resulted from the charge transfer between silicon and carbon atoms. The coulomb effect

Si-sub							
Ni _s	3s	3p	4s	5s	3d	4d	4p
occ.	1.999	6.006	0.396	-0.010	8.463	0.103	0.523
spin	0.000	0.000	0.000	0.000	0.000	0.000	0.000
C ₃							
1s	2s	3s	2p	3p	3d		
occ.	2.000	1.355	0.003	3.248	0.013	0.027	
spin	0.000	0.000	0.000	0.000	0.000	0.000	
C ₁							
1s	2s	3s	2p	3p	3d		
occ.	2.000	1.331	0.002	3.266	0.005	0.027	
spin	0.000	0.000	0.000	0.000	0.000	0.000	
C-sub							
Ni _s	3s	3p	4s	5s	3d	4d	4p
occ.	1.999	6.013	0.560	-0.002	8.781	0.128	0.545
spin	0.000	0.000	0.000	0.000	0.000	0.000	0.000
Si ₃							
2s	2p	3s	4s	3p	4p	3d	
occ.	1.999	6.000	0.978	-0.009	2.067	-0.019	0.513
spin	0.000	0.000	0.000	0.000	0.000	0.000	0.000
Si ₁							
2s	2p	3s	4s	3p	4p	3d	
occ.	1.999	6.000	0.975	-0.010	2.033	-0.020	0.495
spin	0.000	0.000	0.000	0.000	0.000	0.000	0.000

TABLE IV: Projected occupations of Ni_s and NN atoms in Si-sub and C-sub cases.

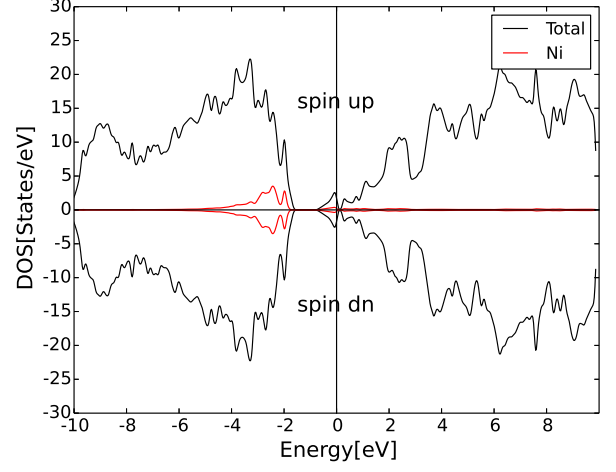
from the NN carbons pushes the defect level towards the valence band. The broadened peak of the defect states compared with that in cubic SiC is due to the lowering of symmetry. The bonding mechanism in 4H-SiC is essentially the same as cubic SiC except for the crystal splitting as shown in Fig.1(b).

The strain dependences of Heisenberg exchange energy in C-sub and Si-sub cases are plotted in Fig.11. For both Ni_{Si} and Ni_C, there's no FM-AFM transition happening as we saw in the 3C-SiC. As the strain is raised from -10% to +6%, the exchange energy increases linearly with a rising rate of 0.0011 %/meV. This is mainly due to that the increasing hopping probability as the Ni-NN distance can't overcome the crystal field splitting (CFS) so as to fail triggering the magnetic transition. More specifically, the t_2 level is splitted into an a_1 and e levels, of which the degeneracies are two and one respectively. The CFS enegy and spin splitting in a_1 and e levels possess the relationship that: $E_{CFS} > \frac{1}{2}(E_{ex1} + E_{ex2})$. Therefore, the spin-up and spin-dn a_1 levels are fully occupied. The transition will happen only when this inequality is broken.

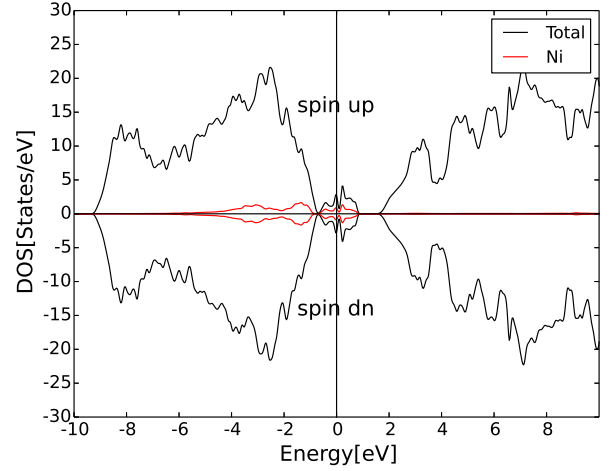
D. Cr in silicon carbide

Except for nickel, other transition-metal single dopants is potential to have similar performance in SiC³¹ due to their characters including:

- the d levels can hybridize with the p orbitals of the dangling bond strongly (t_2 levels) and weakly (e levels)³²;



(a)



(b)

FIG. 10: DOS of C-sub (a) and Si-sub (b) Ni in 4H-SiC.

- the angular momentum 1 triplets won't be splitted due to the high symmetry of the crystal field;
- the larger spin-orbital coupling in d electrons makes high speed electrical field spin manipulation feasible³³.

Therefore, it's worth of exploring the combinations of SiC and other transition-metal elements. Starting from 3C-SiC, the magnetism of chromium dopant comes from the highly localized crystal field splitted e level due to four less electrons compared with nickel. By ordering the active electrons from low to high levels, the t_2 bonding levels are filled and two additional electrons occupies the e levels as shown in Fig.12(a). The stability of Si and C substituted Cr can be evaluated by their formation energy:

$$E^f[X] = E_{tot}[X] - E_p + \mu_{Ni} - \mu_X, \quad (7)$$

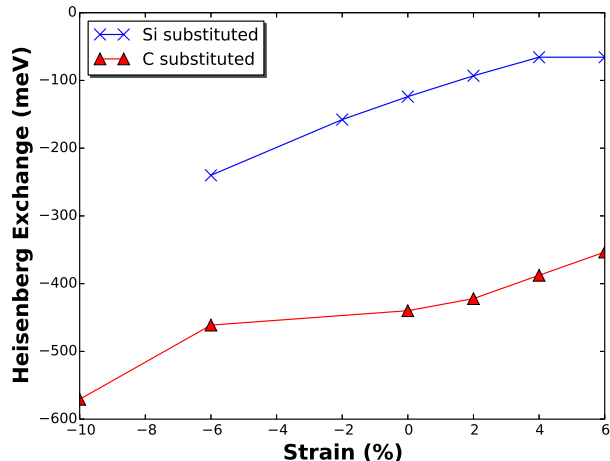


FIG. 11: Strain dependence of the Heisenberg exchange energy.

where E_p is the total energy of pure SiC, μ_{Ni} and μ_X are the chemical potentials of Ni and substituted atom X. The chemical potentials of atoms are chosen to be the values of their bulk materials. Without an external stress, the E^f of Si-sub Cr (1.16 eV) is much lower than that of C-sub Cr (7.72 eV), which indicates that most of the substitutional Cr complexes are formed in the Si sites.

This bonding mechanism can be verified by looking at the DOS shown in Fig.13. Here, all the setup is the same as that in nickel calculation. In the C-sub case (Fig.13a), the localized e levels are located in the middle of the bandgap coinciding with t_2 levels, which is different from Ni dopant. In the Si-sub case (Fig.13a), the electronic structure resembles the Ni dopant to a very high extent. The majority e level is located in the middle of bandgap. But the minority e level (2 eV) is pushed into the conduction band due to the much narrower bandgap compared with diamond. The narrow peak of this e level implies it's highly localized. As a result, the spin residing in Cr complex is mainly assigned to the localized e levels. Our calculation also shows that this property makes the spin state insensitive to the applied strain, which holds in both Si and C substituted case. The two unoccupied t_2 can be clearly observed at 1.7 eV and 2.5 eV. The spin-up and spin-down t_2 states are spread around and hybridize with the e states. The optical spin-flip transition from e up and e down state is feasible due to the spin-orbit interaction, which can mix the e down and t_2 states. This transition indicates quite a bit of potential for manipulating the spin system in its excited states

Compared with the 3C-SiC, the C_{3v} symmetry of 4H-SiC gives rise to a more complicated electronic configura-

tion. As shown in Fig.12(b), the t_2 level in T_d symmetry is splitted up to a e and down to a_1 levels. Again, the detailed electronic configuration can be verified in the DOS shown in Fig.14. The localized e pair remains unchanged

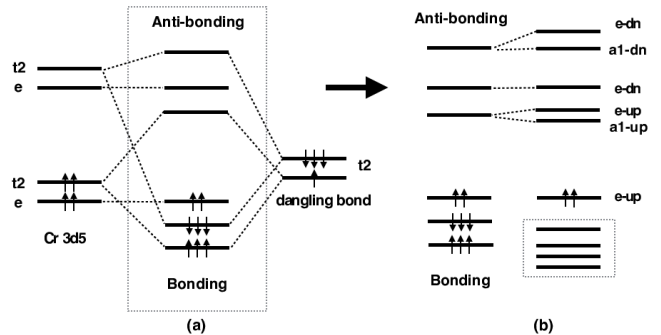


FIG. 12: Electron configuration of Cr doped SiC. (a) Bonding mechanism of silicon substituted Cr in 3C-SiC; (b) Level splitting due to symmetry lowering in 4H-SiC.

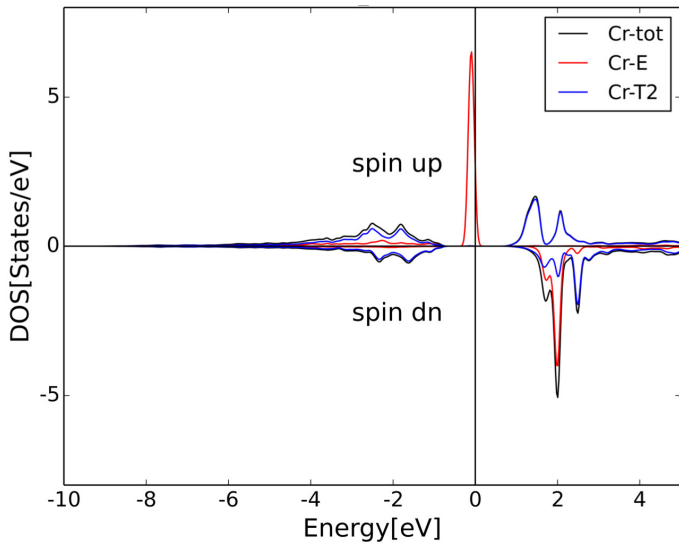
in the bandgap and conduction band. The t_2 derived a_1 can still bridge these two states through spin-orbit interaction.

IV. CONCLUSIONS

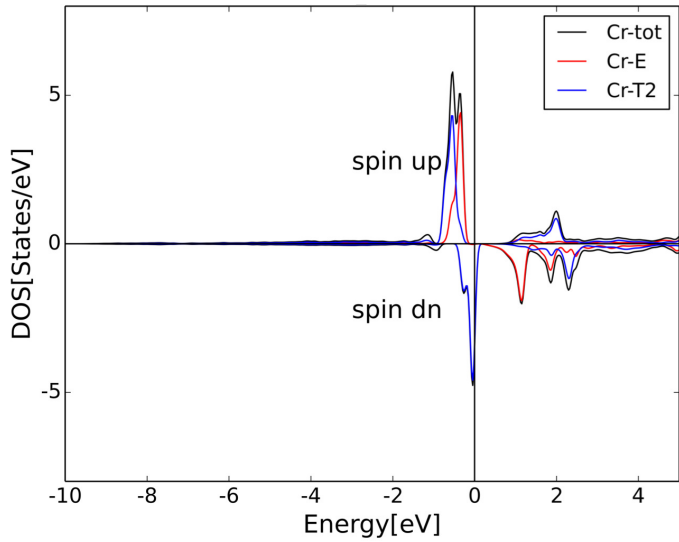
In this paper, we investigated the strain dependence of magnetic property of single substitutional nickel in 3C and 4H SiC with first principles calculation. For 3C-SiC, we observe FM-AFM transitions around 6% tensile hydrostatic strain in C-sub nickel and 10% compressive hydrostatic strain in Si-sub nickel. The Heisenberg exchange-coupling energy is linear to the strain except for a sudden increase at the transition point of C-sub nickel. In contrast, the 4H-SiC doesn't have magnetic phase transition in both substitutional sites but still exhibits a linear relationship between E_{ex} and the strain. Based on the projected orbital occupation through the method of LOMB, we recover the pre-hybridization electron configuration and put it in the $p-d$ hybridization model. We find that a spin pair residing in the substitutional nickel and dangling bond gives rise to the magnetism of the unit cell. By adjusting the distance between the two potential wells, the virtual hopping within the spin pair can be controlled so as to manipulate the spin of the single defect. With an external magnetic field, the qubit can be initialized and manipulated by strain and microwave radiation. Finally, the chromium single dopant in silicon carbide is also investigated. The result shows that a potential d-d spin-flip transition make the spin manipulation feasible in excited states.

¹ J. Isoya, H. Kanda, J. R. Norris, J. Tang, and M. K. Bowman, Phys. Rev. B **41**, 3905 (1990).

² K. Iakoubovskii, Phys. Rev. B **70**, 205211 (2004).



(a)



(b)

FIG. 13: DOS of C-sub (a) and Si-sub (b) Ni in 4H-SiC.

- ³ V. A. Nadolinny, A. P. Yeliseyev, J. M. Baker, M. E. Newton, D. J. Twitchen, S. C. Lawson, O. P. Yuryeva, and B. N. Feigelson, *Journal of Physics: Condensed Matter* **11**, 7357 (1999).
- ⁴ U. Gerstmann, M. Amkreutz, and H. Overhof, *physica status solidi (b)* **217**, 665 (2000).
- ⁵ K. Johnston and A. Mainwood, *Diamond and Related Materials* **12**, 516 (2003), 13th European Conference on Diamond, Diamond-Like Materials, Carbon Nanotubes, Nitrides and Silicon Carbide.
- ⁶ R. N. Pereira, W. Gehlhoff, A. J. Neves, and N. A. Sobolev, *Journal of Physics: Condensed Matter* **15**, 2493 (2003).
- ⁷ T. Gaebel, I. Popa, A. Gruber, M. Domhan, F. Jelezko, and J. Wrachtrup, *New Journal of Physics* **6**, 98 (2004).
- ⁸ J. R. Rabeau, Y. L. Chin, S. Prawer, F. Jelezko, T. Gaebel, and J. Wrachtrup, *Applied Physics Letters* **86**, 131926

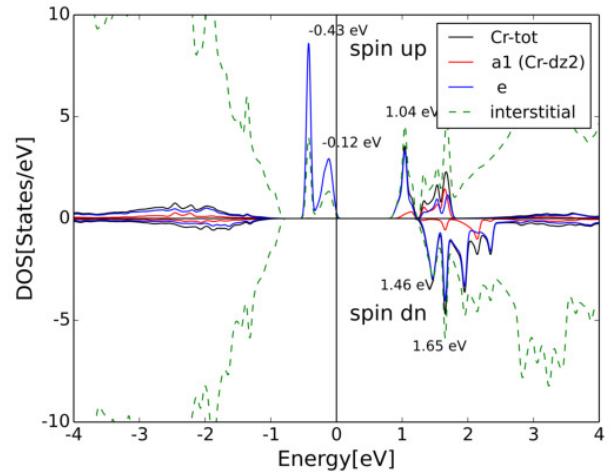


FIG. 14: DOS of Silicon substituted Cr in 4H-SiC.

- (2005), <http://dx.doi.org/10.1063/1.1896088>.
- ⁹ E. Wu, J. R. Rabeau, G. Roger, F. Treussart, H. Zeng, P. Grangier, S. Prawer, and J.-F. Roch, *New Journal of Physics* **9**, 434 (2007).
- ¹⁰ A. POWELL, J. JENNY, S. MULLER, H. McD. HOB-GOOD, V. TSVETKOV, R. LENOARD, and C. CARTER, *International Journal of High Speed Electronics and Systems* **16**, 751 (2006), <http://www.worldscientific.com/doi/pdf/10.1142/S0129156406004016>.
- ¹¹ C. Berger, Z. Song, X. Li, X. Wu, N. Brown, C. Naud, D. Mayou, T. Li, J. Hass, A. N. Marchenkov, E. H. Conrad, P. N. First, and W. A. de Heer, *Science* **312**, 1191 (2006), <http://science.sciencemag.org/content/312/5777/1191.full.pdf>.
- ¹² L. Liu and J. Edgar, *Materials Science and Engineering: R: Reports* **37**, 61 (2002).
- ¹³ N. Mizuochi, S. Yamasaki, H. Takizawa, N. Morishita, T. Ohshima, H. Itoh, and J. Isoya, *Phys. Rev. B* **66**, 235202 (2002).
- ¹⁴ N. T. Son, Z. Zolnai, and E. Jánzén, *Phys. Rev. B* **68**, 205211 (2003).
- ¹⁵ N. T. Son, P. Carlsson, J. ul Hassan, E. Jánzén, T. Umeda, J. Isoya, A. Gali, M. Bockstedte, N. Morishita, T. Ohshima, and H. Itoh, *Phys. Rev. Lett.* **96**, 055501 (2006).
- ¹⁶ A. Gali, *physica status solidi (b)* **248**, 1337 (2011).
- ¹⁷ A. L. Falk, B. B. Buckley, G. Calusine, W. F. Koehl, V. V. Dobrovitski, A. Politi, C. A. Zorman, P. X.-L. Feng, and D. D. Awschalom, *Nat Commun* **4**, 1819 (2013).
- ¹⁸ K. Schwarz, P. Blaha, and G. Madsen, *Computer Physics Communications* **147**, 71 (2002).
- ¹⁹ J. P. Perdew, K. Burke, and M. Ernzerhof, *Phys. Rev. Lett.* **77**, 3865 (1996).
- ²⁰ H. J. Monkhorst and J. D. Pack, *Phys. Rev. B* **13**, 5188 (1976).
- ²¹ T. Chanier, C. E. Pryor, and M. E. Flatt, *EPL (Europhysics Letters)* **99**, 67006 (2012).
- ²² K. Koepf and H. Eschrig, *Phys. Rev. B* **59**, 1743 (1999).
- ²³ G. L. Zhao and D. Bagayoko, *New Journal of Physics* **2**, 16 (2000).

- ²⁴ A. Ferrón, J. L. Lado, and J. Fernández-Rossier, *Phys. Rev. B* **92**, 174407 (2015).
- ²⁵ A. V. Los, A. N. Timoshevskii, V. F. Los, and S. A. Kalkuta, *Phys. Rev. B* **76**, 165204 (2007).
- ²⁶ N. F. Mott, *Philosophical Magazine* **19**, 835 (1969), <http://dx.doi.org/10.1080/14786436908216338>.
- ²⁷ K. Kunc, M. Balkanski, and M. A. Nusimovici, *physica status solidi (b)* **72**, 229 (1975).
- ²⁸ L. Dubrovinsky, N. Dubrovinskaia, E. Bykova, M. Bykov, V. Prakapenka, C. Prescher, K. Glazyrin, H.-P. Liermann, M. Hanfland, M. Ekholm, Q. Feng, L. V. Pourovskii, M. I. Katsnelson, J. M. Wills, and I. A. Abrikosov, *Nature* **525**, 226 (2015).
- ²⁹ M. S. Miao and W. R. L. Lambrecht, *Phys. Rev. B* **74**, 235218 (2006).
- ³⁰ P. w. Anderson, B. I. Halperin, and c. M. Varma, *Philosophical Magazine* **25**, 1 (1972), <http://dx.doi.org/10.1080/14786437208229210>.
- ³¹ T. Chanier, C. Pryor, and M. E. Flatté, *Phys. Rev. B* **86**, 085203 (2012).
- ³² H. P. Hjalmarson, P. Vogl, D. J. Wolford, and J. D. Dow, *Phys. Rev. Lett.* **44**, 810 (1980).
- ³³ J.-M. Tang, J. Levy, and M. E. Flatté, *Phys. Rev. Lett.* **97**, 106803 (2006).